Disentangling orbital and spin exchange interactions for Co^{2+} on a rocksalt lattice

P. M. Sarte,[1,2] R. A. Cowley,[3,*] E. E. Rodriguez,[4] E. Pachoud,[1,2] D. Le,[5] V. García-Sakai,[5] J. W. Taylor,[5]
C. D. Frost,[5] D. Prabhakaran,[3] C. MacEwen,[6] A. Kitada,[7] A. J. Browne,[1,2] M. Songvilay,[2,6] Z. Yamani,[8]
W. J. L. Buyers,[8,9] J. P. Attfield,[1,2] and C. Stock[2,6]
[1]*School of Chemistry, University of Edinburgh, Edinburgh EH9 3FJ, United Kingdom*
[2]*Centre for Science at Extreme Conditions, University of Edinburgh, Edinburgh EH9 3FD, United Kingdom*
[3]*Department of Physics, Clarendon Laboratory, University of Oxford, Park Road, Oxford OX1 3PU, United Kingdom*
[4]*Department of Chemistry and Biochemistry, University of Maryland, College Park, Maryland 20742, USA*
[5]*ISIS Facility, Rutherford Appleton Laboratory, Chilton, Didcot OX11 0QX, United Kingdom*
[6]*School of Physics and Astronomy, University of Edinburgh, Edinburgh EH9 3FD, United Kingdom*
[7]*Department of Materials Science and Engineering, Kyoto University, Yoshida-honmachi, Sakyo, Kyoto 606-8501, Japan*
[8]*National Research Council, Chalk River, Ontario K0J 1JO, Canada*
[9]*Canadian Institute of Advanced Research, Toronto, Ontario M5G 1Z8, Canada*

(Received 23 October 2017; revised manuscript received 16 June 2018; published 17 July 2018)

Neutron spectroscopy was applied to study the magnetic interactions of orbitally degenerate Co^{2+} on a host MgO rocksalt lattice where no long-range spin or orbital order exists. The paramagnetic nature of the substituted monoxide $Co_{0.03}Mg_{0.97}O$ allows for the disentanglement of spin exchange and spin-orbit interactions. By considering the prevalent excitations from Co^{2+} spin pairs, we extract seven exchange constants out to the fourth coordination shell. An antiferromagnetic next-nearest-neighbor 180° exchange interaction is dominant; however, dual ferromagnetic and antiferromagnetic interactions are observed for pairings with other pathways. These interactions can be understood in terms of a combination of orbital degeneracy in the t_{2g} channel and the Goodenough-Kanamori-Anderson rules. Our work suggest that such a hierarchy of exchange interactions exists in transition-metal-based oxides with a t_{2g} orbital degeneracy.

DOI: 10.1103/PhysRevB.98.024415

I. INTRODUCTION

The combination of magnetic exchange and orbital degeneracy has provided the basis for a number of topics in condensed-matter physics including metal-insulator transitions, high-temperature superconductors, colossal magnetoresistance [1–3], and, more recently, Kitaev interactions [4–6]. Rocksalt CoO was the first orbitally degenerate compound to have its magnetic structure investigated using neutron diffraction [7–10], but the underlying exchange interactions are still not known. Indeed, calculations and experiment have been hindered by the complex electronic and orbital ground state of Co^{2+}. While e_g mediated magnetic exchange has been well understood (for example, in $KCuF_3$ [11]), the case of exchange involving degenerate t_{2g} orbitals has proven more difficult [12]. We investigate the magnetic exchange interactions in the case of a t_{2g} orbital degeneracy by performing neutron spectroscopy on MgO substituted with Co^{2+}. We extract seven exchange interactions and observe dual ferro- and antiferromagnetic exchange interactions with comparable magnitudes. The dual exchange interactions are a direct result of the underlying t_{2g} orbital degeneracy of Co^{2+}.

The starting point for understanding the spin-orbital Hamiltonian for paramagnetic Co^{2+} ions is crystal-field theory based on octahedral coordination [13,14] [Fig. 1(a) for rocksalt CoO] [15–17]. As schematically shown in Fig. 1(b), the octahedral crystal field ($\hat{\mathcal{H}}_{CF}$) splits the five degenerate d orbitals (^4F) such that the d^7 electronic structure consists of five electrons occupying the lower-energy t_{2g} states and two electrons in the higher-energy e_g orbitals. This constitutes two orbital triplets ($^4T_{1,2}$) levels separated by $10Dq \sim 900$ meV [17]. The triplet degenerate $^4T_1$ ground state can be approximated to have an effective orbital angular momentum of $\tilde{l} = 1$ [16–24]. Applying spin-orbit coupling (defined by $\hat{\mathcal{H}}_{SO} = \tilde{\lambda}\vec{l} \cdot \vec{S}$, with $S = \frac{3}{2}$) to this orbital ground state results in three effective spin-orbit manifolds classified by an effective angular momentum of $j_{eff} = \frac{1}{2}, \frac{3}{2}$, and $\frac{5}{2}$ (with $\vec{j}_{eff} = \vec{l} + \vec{S}$). The $j_{eff} = \frac{1}{2}$ ground state is separated from the higher-energy $j_{eff} = \frac{3}{2}$ states by $\frac{3}{2}\tilde{\lambda} \sim 36$ meV [17].

In the presence of long-range magnetic order (as exists in CoO at low temperatures), the total single-ion Hamiltonian for Co^{2+} can then be summarized by

$$\hat{\mathcal{H}}_{SI} = \hat{\mathcal{H}}_{CF} + \hat{\mathcal{H}}_{SO} + \hat{\mathcal{H}}_{MF}, \qquad (1)$$

where $\hat{\mathcal{H}}_{CF}$, $\hat{\mathcal{H}}_{SO}$, and $\hat{\mathcal{H}}_{MF}$ are the octahedral crystal-field, spin-orbit, and magnetic-order-induced molecular field. The effect of magnetic ordering on the three spin-orbit manifolds discussed above can be illustrated by considering a single dominant next-nearest-neighbor 180° $Co^{2+} - O^{2-} - Co^{2+}$ superexchange J_2 with

$$\hat{\mathcal{H}}_{MF} = 2J_2 z_2 \langle \hat{\mathbf{S}} \rangle_{av} \hat{\mathcal{S}}^z, \qquad (2)$$

---

[*] Deceased.

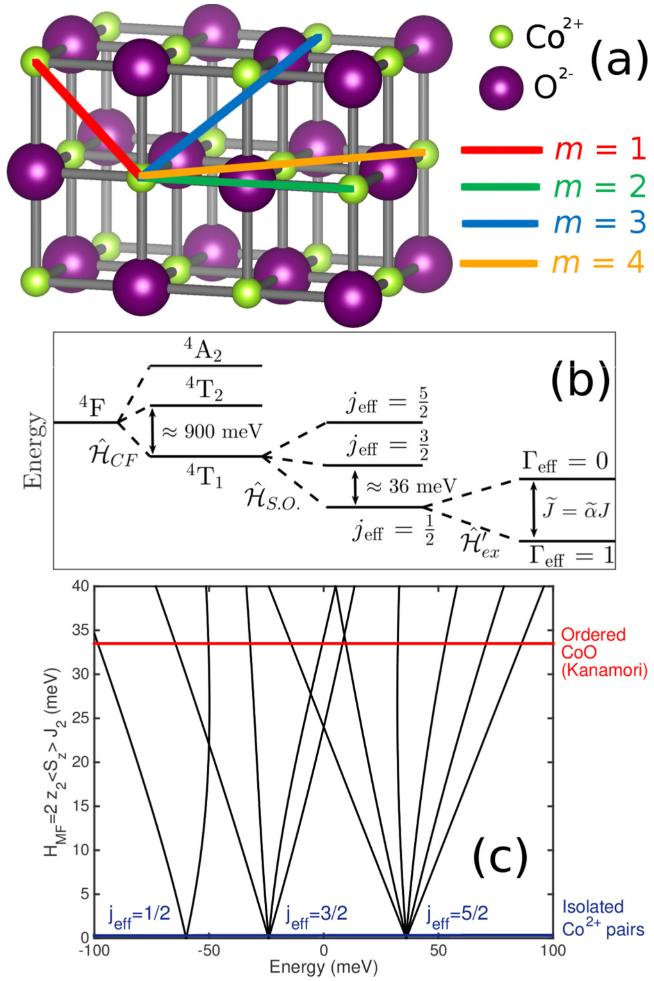

FIG. 1. (a) Cubic (room-temperature) rocksalt $Fm\bar{3}m$ crystal structure of CoO [25]. The pair distances between first shell (nearest) neighbors, second shell (next-nearest) neighbors, etc. are denoted by $m = 1,2$, etc., respectively. (b) The effective pair Hamiltonian $\hat{\mathcal{H}}_{\rm pair}$ for $Co_{0.03}Mg_{0.97}O$. (c) The energy eigenvalues of the single-ion Hamiltonian including a molecular field from magnetic order with Kanamori's estimate [16] of J_2 shown by the solid red line.

where z_2 and $\hat{\mathcal{S}}^z$ denote the number of Co^{2+} neighbors and the z axis of the spin operator [15]. As illustrated in Fig. 1(c), by considering only the predicted value of J_2 by Kanamori [16] in the mean-field expression for $\hat{\mathcal{H}}_{\rm MF}$, a complex admixture of different molecular-field split Co^{2+} spin-orbit manifolds occurs in the presence of magnetic order [15–17].

The strong magnetic-order-induced mixing of multiple $j_{\rm eff}$ manifolds in CoO is in contrast to many other Co^{2+}-based magnets that have both weak exchange and molecular fields and thus exhibit weak mixing [18,26–28]. CoO is further complicated by the possibility of multiple long-range spin-spin interactions [29–32]. The extraction of the multiple-spin exchanges in CoO is thus experimentally very difficult despite the simplicity of its crystal structure [15,17,22,23,30,31,33–35].

We have extracted the magnetic exchange interactions on a rocksalt lattice by investigating weakly substituted $Co_{0.03}Mg_{0.97}O$ using neutron scattering and through considering excitations from the dominant Co^{2+} pair response. This paper is divided into four sections, including this introduction. In Sec. II, we first describe the experimental methods including materials preparation and characterization techniques, where we conclude that our dilute sample can be described by a Co^{2+} pair response. An expanded description of the characterization is given in the Supplemental Material [36], illustrating the x-ray, susceptibility, and energy dispersive x-rays (EDX) data [36]. In Sec. III, the theory required to extract both the exchange constant and the distance associated with the interaction is outlined. We then show the experimental data used to derive the exchange interactions. We finally conclude with a discussion of the results, including a comparison with thermodynamic data from pure CoO, and also how we can understand the results in terms of the Goodenough-Kanamori-Anderson (GKA) rules.

II. EXPERIMENTAL DETAILS AND MATERIALS CHARACTERIZATION

To extract individual J constants for Co^{2+}, we have followed the pioneering work on dilute Mn^{2+} [37,38] and Co^{2+} [22] compounds and measured the dilute monoxide $Co_{0.03}Mg_{0.97}O$ using inelastic neutron spectroscopy. The high magnetic dilution removes the problematic molecular field discussed above [Fig. 1(c)] and suppresses the mixing between $j_{\rm eff}$ manifolds, allowing us to consider a dominant response for Co^{2+} pairs. Probabilistic arguments can be used to illustrate this and are based on the observation that for a given random distribution of xCo^{2+} and $(1-x)Mg^{2+}$ ions, the number of Co^{2+} pairs and the number of pairwise interactions for a given geometry present in the lattice far outweighs the number of Co^{2+} triplets and corresponding interactions between three Co^{2+} cations. For example, if there are N ways that a cluster with a particular geometry of three sites XYZ can occur in a given crystal, the relative probabilities of an arrangement of 3 Mg^{2+}, 1 Co^{2+}, and 2 Mg^{2+} (and its permutations), 2 Co^{2+} and 1 Mg^{2+} (and its permutations), and 3 Co^{2+} occupying the three sites XYZ are $(1-x)^3$, $x(1-x)^2$, $x^2(1-x)$, and x^3, respectively. Hence the ratio of numbers of spin pairs with XY, XZ, and YZ geometry to spin triplets with XYZ geometry in the lattice is $\frac{1-x}{x}$, and thus for small x, the number and hence inelastic neutron-scattering intensities of Co^{2+} pair excitations far outweigh those from larger Co^{2+} clusters. We summarize the sample preparation and characterization techniques confirming the dominant pair response in this section, and an expanded description, including data from the techniques, of the characterization is provided in the Supplemental Material [36]. We also discuss the neutron experiments applied to these materials.

Materials preparation. Two polycrystalline samples of $Co_{0.03}Mg_{0.97}O$ were synthesized for this particular investigation. The first was synthesized by traditional solid-state methods as outlined by Cowley *et al.* [17]. A second sample of $Co_{0.03}Mg_{0.97}O$ was made using solution techniques by mixing stoichiometric amounts of $Mg(NO_3)_2 \times 6H_2O$ and $Co(NO_3)_2 \times 6H_2O$. The solid mixture was dissolved in CH_3CH_2OH and stirred for 1 h and heated to 70 °C for 12 h, yielding a pink gel. The gel was heated in air to 600 °C with a heating rate of 20 °C/h, reacted for 24 h, subsequently heated to 1000 °C with a heating rate of 150 °C/h, held for an additional 48 h, and finally cooled to room temperature by switching off the furnace. Details concerning the synthesis and treatment of MgO and CoO samples are outlined by Cowley *et al.* [17]. We note that both magnetically substituted MgO samples gave consistent results and the comparison is shown in the Supplemental Material [36].

Laboratory x-ray diffraction. Room-temperature powder-diffraction patterns of the end members (CoO and MgO) and $Co_xMg_{1-x}O$ synthesized by sol-gel were collected over $2\theta = [25,100]^\circ$ in 0.02° steps on a Bruker D2 Phaser laboratory x-ray diffractometer utilizing a monochromated Cu $K_{\alpha,1,2}$ source. As illustrated in the Supplemental Material [36], Rietveld refinement of $Mg_{1-x}Co_xO$ indicates that the solid solution assumes a rocksalt structure ($Fm\bar{3}m$) with a unit-cell parameter $a = 4.2131(2)$ Å. Utilizing the measured values of the end members CoO (4.2594(4) Å) and MgO (4.2118(1) Å), the unit-cell parameter of 4.2131(2) Å corresponds to an $x = 0.025(5)$ according to Vegard's law [39], supporting that approximately 3% of the Mg^{2+} sites contain Co^{2+}.

Energy-dispersive x-ray analysis. As a final direct confirmation of the concentration of Co^{2+} in our sample, we performed energy-dispersive x-ray measurements. Elemental analysis was performed using scanning electron microscopy (SEM) on a Hitachi SU-70 Schottky field-emission gun SEM with an equipped Bruker Quantax energy-dispersive x-ray detector. Energy-dispersive x-ray spectroscopy (EDS) was carried out at 15 keV. The results are illustrated in the Supplemental Material [36] show the effective substitution and the homogeneous distribution of cobalt throughout the sample. The spatially resolved analysis also confirms a homogenous distribution of cobalt throughout the sample.

DC magnetic susceptibility. Temperature dependence of magnetization was measured on a Quantum Design MPMS for a 32.5 mg of polycrystalline $Co_{0.03}Mg_{0.97}O$ synthesized by sol-gel in an external dc field $\mu_o H_{\rm ext} = 0.1$ T. Zero-field-cooling (ZFC) measurements were performed in 2 K steps spaced linearly from 2 to 300 K, while FC measurements were performed in 5 K steps spaced linearly from 2 to 170 K. As described in the Supplemental Material [36], the Curie-Weiss constant was found to be consistent with pairs of Co^{2+} with an exchange interaction reported by Kanamori [16]. The Curie constant was found to agree with a concentration of Co^{2+} ions, consistent with starting concentrations, x-ray powder diffraction, and also EDX measurements. Susceptibility measurements therefore confirm the following key experimental properties of our substituted samples: the lack of magnetic ordering; the absence of measurable clustering of Co^{2+} evidenced from no measurable difference between zero-field and field-cooled sweeps; a Curie-Weiss constant consistent with a dominant 180° superexchange interaction; and finally a Curie constant consistent with starting concentrations.

Inelastic neutron-scattering details. 45.8, 45.2, 32.5, and 15.7 g of $Co_{0.03}Mg_{0.97}O$ synthesized by the standard solid-state and sol-gel methods, annealed MgO and CoO, respectively, were placed in separate airtight aluminum cans under helium. The high-energy measurements were made on the direct geometry MARI spectrometer. For measurements concerning the $Co_{0.03}Mg_{0.97}O$ sample synthesized by traditional solid-state methods, MgO and CoO powders, the t_o chopper was operated at 50 Hz in parallel with a Gd chopper spun at frequencies $f = 350$, 250 and 150 Hz with incident energies $E_i = 30$, 10, and 5 meV, respectively, providing an elastic resolution of 0.7, 0.2, and 0.1 meV, respectively. For measurements concerning the $Co_{0.03}Mg_{0.97}O$ sample synthesized by sol-gel, the Gd chopper was spun at $f = 350$ and 250 Hz with an E_i of 29.50 and 14.50 meV, providing an elastic resolution of 0.7 and 0.2 meV, respectively. For both $Co_{0.03}Mg_{0.97}O$ samples, a thick disk chopper with $f = 50$ Hz reduced the background from high-energy neutrons. A top-loading Displex CCR cooled the samples to a base temperature of approximately 5 K. We note that further neutron inelastic scattering results comparing pure MgO, CoO, and our substituted MgO sample are presented in the Supplemental Material [36].

For lower energies, measurements were made on the indirect geometry IRIS spectrometer. The final energy was fixed at 1.84 meV by PG002 analyzer crystals in near backscattering geometry. The graphite analyzers are cooled to reduce thermal diffuse scattering, providing an elastic resolution of 17.5 μeV. A combination of IRIS' long path length and its array of disk choppers allowed us to select multiple time windows, resulting in the measured bandwidth being selectively increased to include energy transfers up to ~2 meV. A top-loading Displex CCR was used to cool the sample to a base temperature of approximately 11 K. For all samples, identical instrumental and environmental parameters were employed on IRIS.

III. Co^{2+} PAIR INTERACTIONS

Having discussed the materials preparation and characterization, we conclude that our rocksalt MgO sample substituted with Co^{2+} can be considered to be dominated by pairs of Co^{2+} ions. We now discuss the neutron-scattering response of an isolated pair of magnetic ions and how it can be used to extract both the interaction distance and also the energy-exchange interaction. By considering Co^{2+} pair interactions and only low-energy excitations within the lowest $j_{\rm eff} = \frac{1}{2}$ doublet (with $\hat{\tilde{\mathbf{j}}} = \beta\hat{\mathbf{S}}$), the interaction energy $\hat{\mathcal{H}}_{\rm ex}$ between a pair of Co^{2+} ions in substituted $Mg_{0.97}Co_{0.03}O$ is approximated by

$$\hat{\mathcal{H}}'_{\rm ex} = 2J\hat{\mathbf{S}}_1 \cdot \hat{\mathbf{S}}_2 \sim \tilde{\alpha} J \hat{\tilde{\mathbf{j}}}_1 \cdot \hat{\tilde{\mathbf{j}}}_2, \tag{3}$$

where $\hat{\tilde{\mathbf{j}}}$ and $\tilde{\alpha} = 2\beta^2$ denote an effective total angular momentum operator with $j = \frac{1}{2}$ and a projection factor, respectively. As summarized by Fig. 1(b), the $\hat{\mathcal{H}}'_{\rm ex}$ describes individual $j_{\rm eff} = \frac{1}{2}$ pair excitations as transitions between triplet ($\Gamma_{\rm eff} = 1$) and singlet ($\Gamma_{\rm eff} = 0$) levels separated by an energy of $\Delta E = \tilde{\alpha} J$ [43–45]. The projection factor $\tilde{\alpha}$, in this low-energy approximation, can be calculated by diagonalizing $\hat{\mathcal{H}}_{\rm SI} + \hat{\mathcal{H}}'_{\rm ex}$, with $\hat{\mathcal{H}}_{\rm MF} = 0$ owing to the lack of long-range magnetic order in $Co_{0.03}Mg_{0.97}O$ [17]. This is equivalent to the following Hamiltonian for two (labeled 1 and 2) interacting Co^{2+} ions:

$$\hat{\mathcal{H}}' = \tilde{\lambda}\hat{\tilde{\mathbf{l}}}_1 \cdot \hat{\mathbf{S}}_1 + \tilde{\lambda}\hat{\tilde{\mathbf{l}}}_2 \cdot \hat{\mathbf{S}}_2 + 2J\hat{\mathbf{S}}_1 \cdot \hat{\mathbf{S}}_2. \tag{4}$$

By considering $\tilde{l} = 1$ and $S = \frac{3}{2}$, this amounts to 144 basis states and a 144 × 144 matrix for this particular Hamiltonian in terms of the two-particle basis of $|\tilde{l}_1, m_{\tilde{l},1}, s_1, m_{s,1}\rangle \otimes$

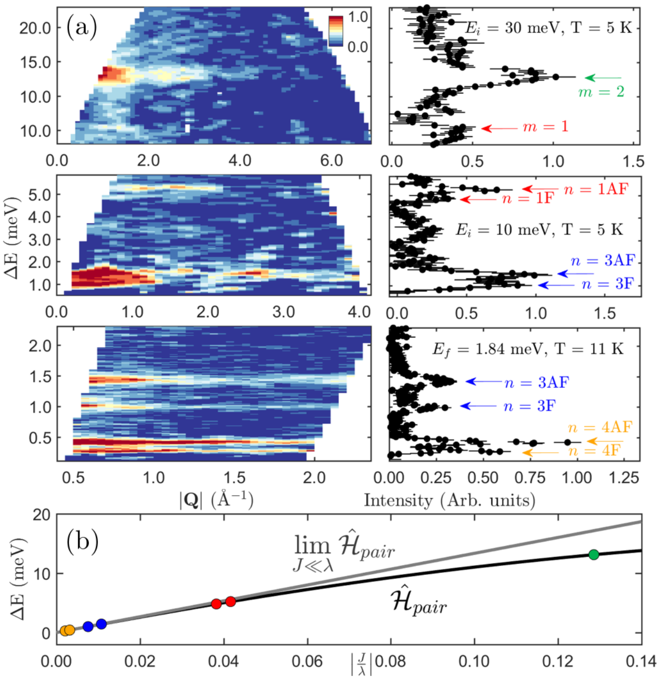

FIG. 2. (a) Background (using pure and nonmagnetic MgO) subtracted powder-averaged neutron-scattering intensity maps of $\mathrm{Co_{0.03}Mg_{0.97}O}$ measured on (a, top left) MARI at 5 K with an $E_i = 30$ meV, (a, middle left) MARI at 5 K with an $E_i = 10$ meV and (a, bottom left) IRIS at 11 K with an E_f of 1.84 meV revealing seven low-energy bands of dispersionless magnetic excitations. The right column shows $|\mathbf{Q}|$-integrated cuts. Labels denote the coordination shell m and the type of coupling present with label n, both of which are determined in Fig. 3. (b) The black curve denotes the pair energy splitting as a function of the normalized exchange $\Delta E(|\frac{J}{\lambda}|)$. The points are measured energy positions from (a). The gray line is the same relationship derived using the projection theorem in the large-λ limit [19,20].

$|\tilde{l}_2, m_{\tilde{l},2}, s_2, m_{s,2}\rangle$, where $\tilde{l}_i$, $m_{\tilde{l},i}$, s_i, and $m_{s,i}$ denote the eigenvalues corresponding to the $\hat{\tilde{\mathbf{l}}}_i$, $\hat{\tilde{\mathbf{l}}}_{z,i}$, $\hat{\mathbf{S}}_i$, and $\hat{\mathbf{S}}_{z,i}$ operators, respectively, for the ith particle. As illustrated in Fig. 2(b), in the limit of $J \ll \lambda$, $\Delta E(J)$ is linear with $\tilde{\alpha} = \frac{50}{9}$, in agreement with the projection theorem of angular momentum [20,44]. Therefore, measuring pair excitations with neutron spectroscopy provides a direct way to estimate the magnitude of exchange constant $|J|$ between neighboring $\mathrm{Co^{2+}}$ ions when this projection factor is taken into account. We note that this is independent of the sign of J and we discuss how that can be determined from the temperature dependence below.

While the excitation energy provides the magnitude $|J|$, the neutron spectroscopic momentum dependence can be used to extract the corresponding intrapair distance $\mathbf{R}_m$, where m denotes the coordination shell. By applying the Hohenberg-Brinckman first-moment sum rule and the single-mode approximation for an isolated pair, excitations from a $\mathrm{Co^{2+}}$ pair have the following $|\mathbf{Q}|$ dependence [43,50,51]:

$$S(|\mathbf{Q}|) \propto \frac{|F(|\mathbf{Q}|)|^2}{\Delta E_o}\left(1 - \frac{\sin(|\mathbf{Q}||\mathbf{R}_m|)}{|\mathbf{Q}||\mathbf{R}_m|}\right), \tag{5}$$

with $|F(|\mathbf{Q}|)|^2$ the magnetic form factor. Since the modulation is solely dependent on the intrapair distance $\mathbf{R}_m$, the excitation can be assigned to a particular pair and corresponding coordination shell in the $Fm\bar{3}m$ structure, as illustrated in Fig. 1(a).

IV. RESULTS AND DISCUSSION

Having discussed the theory for isolated pairs in dilute $\mathrm{Co_{0.03}Mg_{0.97}O}$, we now present the experimental data. As illustrated by Fig. 2(a), low-temperature/incident-energy inelastic neutron spectroscopic measurements on powder $\mathrm{Co_{0.03}Mg_{0.97}O}$ display a hierarchy of dispersionless excitations up to $\Delta E \sim 15$ meV. Based on the energy value of the excitations, we can assign an exchange constant as shown in Fig. 2(b) using the previously measured value for the spin-orbit-coupling constant $\tilde{\lambda}$ [17] for isolated $\mathrm{Co^{2+}}$ on a rocksalt lattice. The intensities for each of the seven excitations in Fig. 2(a) exhibit a modulated $|\mathbf{Q}|$ dependence, characteristic of pairwise interactions and thus distinguishing them from single-ion dispersionless crystal-field excitations [43]. As shown in Figs. 3(a) and 3(b), by fitting the intensity of each mode at different energies to Eq. (5), the different pair excitations could be assigned to relative coordination shells ranging from $m = 1$ to $m = 4$.

We now discuss the temperature dependence with the goal of extracting the sign of J. Antiferromagnetically coupled ($J > 0$) pairs of $j_{\text{eff}} = \frac{1}{2}$ spins consist of a singlet ground state and a triplet excited state, while ferromagnetic coupling ($J < 0$) gives a triplet ground state and a single excited state. These two different coupling scenarios give distinct temperature dependences of the integrated intensity that scales as the thermal population difference between the ground and excited states [51,52], with antiferromagnetic pairs following

$$I_{\text{AF}}(T) \propto (1 - e^{-\Delta E/k_BT})/(1 + 3e^{-\Delta E/k_BT}) \tag{6}$$

and ferromagnetic pairs following

$$I_{\text{F}}(T) \propto (1 - e^{-\Delta E/k_BT})/(3 + e^{-\Delta E/k_BT}), \tag{7}$$

such that as $T \to 0$ K, the ratio

$$\frac{I_{\text{AF}}}{I_{\text{F}}} = \frac{3 + e^{-\Delta E/k_BT}}{1 + 3e^{-\Delta E/k_BT}} \to 3. \tag{8}$$

As illustrated in Fig. 3(d), by normalizing the temperature dependence by $I_{\text{F}}(T)$, all integrated intensities fall onto either one of two universal curves describing antiferromagnetism or ferromagnetism.

All extracted values of J based on the energy, momentum, and temperature dependence discussed above are summarized in Table I. All coordination shells, with the exception of $m = 2$, display two closely spaced excitations with differing signs for the exchange constant, as illustrated in Fig. 3(c) for the ~5 meV excitation. This presence of dual ferro- and antiferromagnetic interactions for $m = 1$, 3, and 4 is consistent with the GKA rules [40–42,53] since each of these exchange pathways consists of at least one 90° $\mathrm{Co^{2+}} - \mathrm{Co^{2+}}$ interaction involving the overlap of half and filled orbitals. Indeed, the GKA rules predict that the combination of the orbital degree of freedom for *each* $\mathrm{Co^{2+}}$ and a lack of orbital ordering (or anisotropy) would manifest itself as either a direct antiferromagnetic ${t_{2g}}^1 - {t_{2g}}^1$ or a weaker ferromagnetic

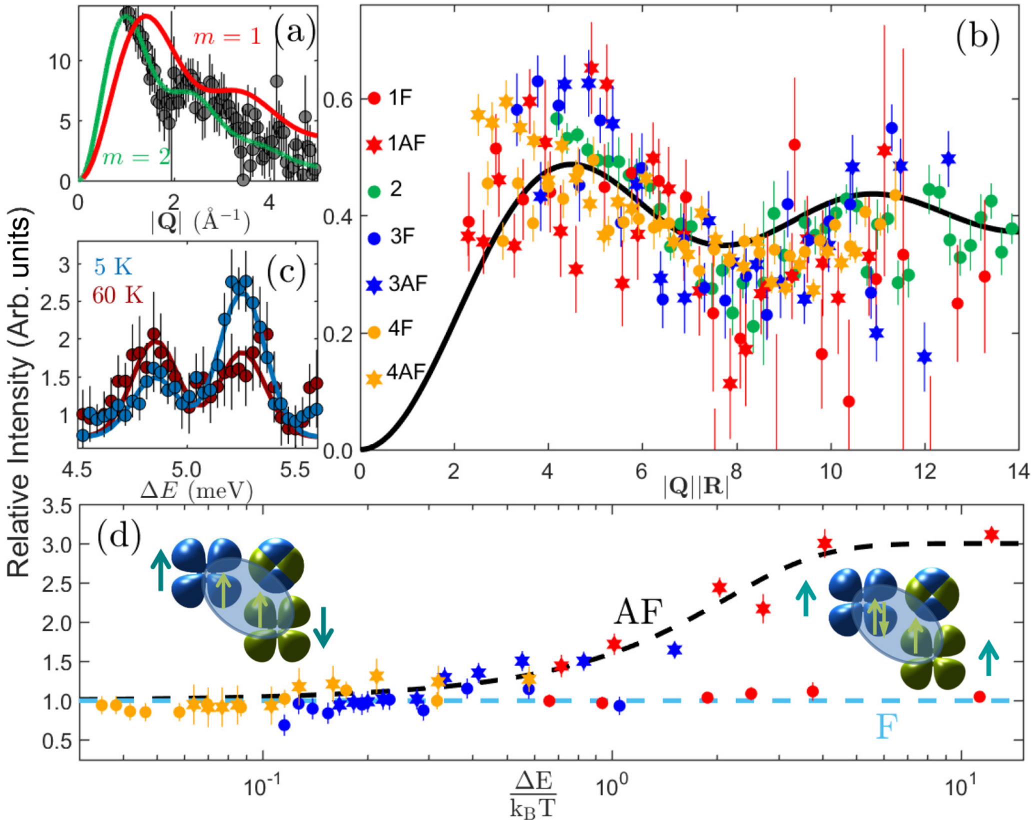

FIG. 3. (a) Constant-E cut ($\Delta E = [12,14]$ meV) from MARI at 5 K with an $E_i = 30$ meV. The green curve is a fit to Eq. (5) with $|\mathbf{R}| = 4.2(3)$ Å ($m = 2$ pairs). The red curve is with $|\mathbf{R}|$ fixed as 2.98 Å ($m = 1$ pairs). (b) Scaled and form-factor-corrected $|\mathbf{Q}|$ dependence of the intensities for all magnetic excitations with $|\mathbf{R}|$ calculated from the fitting routine described in (a). The solid black curve is $1 - \frac{\sin(|\mathbf{Q}||\mathbf{R}_n|)}{|\mathbf{Q}||\mathbf{R}_n|}$. (c) Constant-$|\mathbf{Q}|$ cut (MARI, $E_i = 10$ meV) showing a different temperature dependence for the two peaks despite both being from $m = 1$ pairs. (d) Normalized temperature dependence of the Bose-factor-corrected integrated intensity for all seven excitations (Fig. 2) showing two universal curves calculated (dashed lines) for antiferromagnetic and ferromagnetic coupling. Both the integrated intensities and the calculated behavior of antiferromagnetic or ferromagnetically coupled pairs were normalized by $I_{\mathrm{F}}(T)$, as described in the main text. The inset is a pictorial representation of the sign of J as predicted by the GKA rules [40–42]—antiferromagnetism (left) is a result of exchange between two half-filled and completely filled t_{2g} orbitals, while weaker ferromagnetism (right) is a result of exchange between a half-filled and completely filled t_{2g} orbitals. Yellow arrows denote local t_{2g} spin configurations and teal arrows denote total spin configurations on each Co^{2+}.

${t_{2g}}^1 - {t_{2g}}^2$ exchange interaction. As summarized in Fig. 3(d) and Table I, the experimental results verify the GKA rules [40–42,53] as the antiferromagnetic interaction is stronger than the ferromagnetic alternative for all the $m \neq 2$ excitations, while the 180° $\mathrm{Co}^{2+} - \mathrm{O}^{2-} - \mathrm{Co}^{2+}$ m = 2 coupling leads to only a strong antiferromagnetic interaction.

Having assigned the signs of the seven exchange constants for dilute $\mathrm{Co}_{0.03}\mathrm{Mg}_{0.97}\mathrm{O}$, we now provide a comparison with thermodynamic data and previously measured and calculated exchange constants for bulk CoO. The additional complication of dual ferro- and antiferromagnetic interactions for most m exchange pathways in combination with the entanglement of individual spin-orbit manifolds in the presence of magnetic order provides a possible explanation for the large range of J values reported for CoO [16,30,31,35,54–58]. As summarized in Table I, the values of J show good agreement with three general trends reported by experiment [30]: (i) dominant $J_2 > 0$, (ii) a $J_1 < 0$, and (iii) a significantly smaller but non-negligible J_3, all in broad agreement with the trends concluded from a recent generalized gradient approximation (GGA)+U density functional theory (DFT) calculation on CoO (though no such dual exchange was predicted) [32]. In terms of thermodynamic data, the Curie-Weiss constant is related to the exchange interactions via $\Theta_{\mathrm{CW}} = -\frac{2}{3}S(S+1)\sum_i z_i J_i$, where the spin value $S = \frac{3}{2}$ and z_i is the number of neighbors for each ith exchange interaction [48,49]. Following Kanamori [16] and applying a correction for spin-orbit coupling, the effective Curie-Weiss temperature $\widetilde{\theta}_{\mathrm{CW}}$ is listed in Table I and compared against a mean-field T_N calculated based just on J_2. The estimated $\widetilde{\theta}_{\mathrm{CW}}$ of $-295(5)$ K [$-25.4(5)$ meV] and a mean-field estimate of T_{N} of 283(5) K [24.4(3) meV] demonstrate close similarities with experimentally determined values of $\theta_{\mathrm{CW}} = -330(4)$ K [46,47] and $T_N = 291(4)$ K [25], respectively, for CoO. The excellent agreement results from the near-perfect cancellation of antiferromagnetic and ferromagnetic interactions for all coordinations with the exception of $m = 2$ (the 180° interaction). Although the $\mathrm{Co}_{0.03}\mathrm{Mg}_{0.97}\mathrm{O}$ lattice ($a = 4.21$ Å) is contracted relative to that of pure CoO ($a = 4.26$ Å), the above agreements of energy scale are highly suggestive that the $\mathrm{Co}^{2+} - \mathrm{Co}^{2+}$ exchange interactions are not greatly

TABLE I. Magnetic exchange constants for $Co_{0.03}Mg_{0.97}O$ determined by the current study, magnetic exchange constants for CoO as cited in literature [30,31], and calculated for CoO by Deng *et al.* [32] using GGA+U DFT. The values from GGA+U DFT have been renormalized such that J_2 is equal to the value from this current study. The values of T_N, θ_{CW}, and λ reported in the literature [17,25,46,47] for CoO have been included for the purposes of a comparison to the mean-field value [48,49] of θ_{CW} corresponding to the J values determined by the current study.

Quantity/Source	Current study (meV)	Literature studies (meV)	Calculated (meV) [32]
$\tilde{\lambda}$		24(5) [17]	
J_{1AF}	1.000(8)	0.60 to − 0.31 [16,30]	−0.97(2)
J_{1F}	−0.918(6)		
J_2 or J_{2AF}	3.09(5)	2.8 to 0.0013 [30]	3.09(5)
J_{3AF}	0.258(1)	−0.67 [31]	−0.461(8)
J_{3F}	−0.182(1)		
J_{4AF}	0.0759(4)		−0.0085(1)
J_{4F}	−0.0504(4)		
T_N	24.4(3)[a]	25.1(4) [25]	
θ_{CW}	−25.4(5)	−28.4(4) [46,47]	

[a] Calculated using the mean-field estimate $T_N \sim |\frac{2}{3}S(S+1)z_2J_2|$.

changed, or at least any changes are smaller than systematic errors introduced by attempting to simplify the scheme in pure CoO. Hence the present results represent a comprehensive set of interaction-energy estimates for CoO.

In summary, we have disentangled the exchange and spin-orbit interactions for Co^{2+} on a rocksalt lattice. Through a combined analysis of the energy, momentum, and temperature dependence, we have extracted seven exchange constants out to four coordination shells. Both ferro- and antiferromagnetic interactions are observed, with the exception of second-neighbor interactions through linear $Co^{2+} - O^{2-} - Co^{2+}$ bridges, in agreement with both the GKA rules and thermodynamic data. The results demonstrate that in the case of an orbital degeneracy in the t_{2g} channel, dual ferro- and antiferromagnetic interactions occur with comparable magnitudes.

ACKNOWLEDGMENTS

We acknowledge useful conversations with T. Guidi, J. R. Stewart, M. A. Green, T. J. Williams, K. H. Hong, G. M. McNally, and S. E. Maytham. We are grateful to the Carnegie Trust for the Universities of Scotland, the Royal Society, the STFC, the ERC, and the EPSRC for financial support. P.M.S. acknowledges financial support from the CCSF and the University of Edinburgh through the GRS and PCDS.

---

[1] Y. Tokura and N. Nagaosa, Science **288**, 462 (2000).
[2] E. Dagotto, Science **309**, 257 (2005).
[3] K. I. Kugel and D. I. Khomskii, Sov. Phys. JETP **136**, 621 (1982).
[4] Y. Okamoto, M. Nohara, H. A. Katori, and H. Takagi, Phys. Rev. Lett. **99**, 137207 (2007).
[5] R. Wang, A. Go, and A. J. Millis, Phys. Rev. B **95**, 045133 (2017).
[6] G. Jackeli and G. Khaliullin, Phys. Rev. Lett. **102**, 017205 (2009).
[7] C. G. Shull, W. A. Strauser, and E. O. Wollan, Phys. Rev. **83**, 333 (1951).
[8] Y. Y. Li, Phys. Rev. **100**, 627 (1955).
[9] W. L. Roth, Phys. Rev. **110**, 1333 (1958).
[10] B. van Laar, Phys. Rev. **138**, A584 (1965).
[11] S. K. Satija, J. D. Axe, G. Shirane, H. Yoshizawa, and K. Hirakawa, Phys. Rev. B **21**, 2001 (1980).
[12] A. M. Oles, P. Horsch, L. F. Feiner, and G. Khaliullin, Phys. Rev. Lett. **96**, 147205 (2006).
[13] M. W. Haverkort, A. Tanaka, L. H. Tjeng, and G. A. Sawatzky, Phys. Rev. Lett. **99**, 257401 (2007).
[14] B. C. Larson, W. Ku, J. Z. Tischler, C.-C. Lee, O. D. Restrepo, A. G. Eguiluz, P. Zschack, and K. D. Finkelstein, Phys. Rev. Lett. **99**, 026401 (2007).
[15] J. Sakurai, W. J. L. Buyers, R. A. Cowley, and G. Dolling, Phys. Rev. **167**, 510 (1968).
[16] J. Kanamori, Prog. Theor. Phys. **17**, 177 (1957).
[17] R. A. Cowley, W. J. L. Buyers, C. Stock, Z. Yamani, C. Frost, J. W. Taylor, and D. Prabhakaran, Phys. Rev. B **88**, 205117 (2013).
[18] F. Wallington, A. M. Arévalo-Lopez, J. W. Taylor, J. R. Stewart, V. García-Sakai, J. P. Attfield, and C. Stock, Phys. Rev. B **92**, 125116 (2015).
[19] D. I. Khomskii, *Transition Metal Compounds* (Cambridge University Press, Cambridge, 2014).
[20] A. Abragam and B. Bleaney, *Electron Paramagnetic Resonance of Transition Ions* (Oxford University Press, Oxford, 2012).
[21] J. Kanamori, Prog. Theor. Phys. **17**, 197 (1957).
[22] W. J. L. Buyers, T. M. Holden, E. C. Svensson, R. A. Cowley, and M. T. Hutchings, J. Phys. C: Solid State Phys. **4**, 2139 (1971).
[23] W. J. L. Buyers, T. M. Holden, E. C. Svensson, and D. J. Lockwood, Phys. Rev. B **30**, 6521 (1984).
[24] R. A. Cowley, W. J. L. Buyers, P. Martel, and R. W. H. Stevenson, J. Phys. C: Solid State Phys. **6**, 2997 (1973).
[25] W. Jauch, M. Reehuis, H. J. Bleif, F. Kubanek, and P. Pattison, Phys. Rev. B **64**, 052102 (2001).
[26] R. Coldea, D. A. Tennant, E. M. Wheeler, E. Wawrzynska, D. Prabhakaran, M. Telling, K. Habicht, P. Smeibidl, and K. Kiefer, Science **327**, 177 (2010).

[27] B. Grenier, S. Petit, V. Simonet, E. Canévet, L.-P. Regnault, S. Raymond, B. Canals, C. Berthier, and P. Lejay, Phys. Rev. Lett. **114**, 017201 (2015).

[28] H. D. Zhou, C. Xu, A. M. Hallas, H. J. Silverstein, C. R. Wiebe, I. Umegaki, J. Q. Yan, T. P. Murphy, J.-H. Park, Y. Qiu, J. R. D. Copley, J. S. Gardner, and Y. Takano, Phys. Rev. Lett. **109**, 267206 (2012).

[29] A. L. Dalverny, J. S. Filhol, F. Lemoigno, and M. L. Doublet, J. Phys. Chem. C **114**, 21750 (2010).

[30] M. Feygenson, X. Teng, S. E. Inderhees, Y. Yiu, W. Du, W. Han, J. Wen, Z. Xu, A. A. Podlesnyak, J. L. Niedziela, M. Hagen, Y. Qiu, C. M. Brown, L. Zhang, and M. C. Aronson, Phys. Rev. B **83**, 174414 (2011).

[31] K. Tomiyasu and S. Itoh, J. Phys. Soc. Jpn. **75**, 084708 (2006).

[32] H.-X. Deng, J. Li, S.-S. Li, J.-B. Xia, A. Walsh, and S.-H. Wei, Appl. Phys. Lett. **96**, 162508 (2010).

[33] Z. Yamani, W. J. L. Buyers, R. A. Cowley, and D. Prabhakaran, Can. J. Phys. **88**, 729 (2010).

[34] G. Fischer, M. Däne, A. Ernst, P. Bruno, M. Lüeders, Z. Szotek, W. Temmerman, and W. Hergert, Phys. Rev. B **80**, 014408 (2009).

[35] C. Kant, T. Rudolf, F. Schrettle, F. Mayr, J. Deisenhofer, P. Lunkenheimer, M. V. Eremin, and A. Loidl, Phys. Rev. B **78**, 245103 (2008).

[36] See Supplemental Material at http://link.aps.org/supplemental/10.1103/PhysRevB.98.024415 for a description of sample characterization.

[37] A. Furrer, A. Podlesnyak, and K. W. Krämer, Phys. Rev. B **92**, 104415 (2015).

[38] E. C. Svensson, M. Harvey, W. J. L. Buyers, and T. M. Holden, J. Appl. Phys. **49**, 2150 (1978).

[39] L. Vegard, Z. Phys. **5**, 17 (1921).

[40] J. B. Goodenough, J. Phys. Chem. Solids **6**, 287 (1958).

[41] J. Kanamori, J. Phys. Chem. Solids **10**, 87 (1959).

[42] P. W. Anderson, Phys. Rev. **79**, 350 (1950).

[43] J. T. Haraldsen, T. Barnes, and J. L. Musfeldt, Phys. Rev. B **71**, 064403 (2005).

[44] M. Rose, *Elementary Theory of Angular Momentum, Dover Books on Physics and Chemistry* (Dover, New York, 1995).

[45] A. Furrer and O. Waldmann, Rev. Mod. Phys. **85**, 367 (2013).

[46] T. Nagamiya, K. Yosida, and R. F. Kubo, Adv. Phys. **4**, 1 (1955).

[47] J. R. Singer, Phys. Rev. **104**, 929 (1956).

[48] K. Lee, J. Lee, C. Lee, and M. Whangbo, Bull. Korean Chem. Soc. **35**, 1277 (2014).

[49] C. Kittel, *Introduction to Solid State Physics* (Wiley, New York, 2005).

[50] P. C. Hohenberg and W. F. Brinkman, Phys. Rev. B **10**, 128 (1974).

[51] M. B. Stone, M. D. Lumsden, S. Chang, E. C. Samulon, C. D. Batista, and I. R. Fisher, Phys. Rev. Lett. **100**, 237201 (2008).

[52] Y. Zhu, *Modern Techniques for Characterizing Magnetic Materials* (Springer Science & Business Media, New York, 2005).

[53] J. B. Goodenough, Phys. Rev. **100**, 564 (1955).

[54] M. Tachiki, J. Phys. Soc. Jpn. **19**, 454 (1964).

[55] M. El-Batanouny, J. Phys.: Condens. Matter **14**, 6281 (2002).

[56] H.-h. Chou and H. Y. Fan, Phys. Rev. B **13**, 3924 (1976).

[57] R. R. Hayes and C. H. Perry, Solid State Commun. **13**, 1915 (1973).

[58] T. Satoh, R. Iida, T. Higuchi, Y. Fujii, A. Koreeda, H. Ueda, T. Shimura, K. Kuroda, V. I. Butrim, and B. A. Ivanov, Nat. Commun. **8**, 638 (2017).